

The meillers Autunian hydrothermal chalcedony : first evidence of a similar to 295 Ma auriferous epithermal sinter in the Frech Massif Central.

Eric Marcoux, P. Le Berre, Alain Cocherie

▶ **To cite this version:**

Eric Marcoux, P. Le Berre, Alain Cocherie. The meillers Autunian hydrothermal chalcedony : first evidence of a similar to 295 Ma auriferous epithermal sinter in the Frech Massif Central.. Ore Geology Reviews, 2004, 25, pp.1-2 69-87. 10.1016/j.oregeorev.2003.10.001 . hal-00068297

HAL Id: hal-00068297

https://insu.hal.science/hal-00068297

Submitted on 19 May 2006

HAL is a multi-disciplinary open access archive for the deposit and dissemination of scientific research documents, whether they are published or not. The documents may come from teaching and research institutions in France or abroad, or from public or private research centers.

L'archive ouverte pluridisciplinaire **HAL**, est destinée au dépôt et à la diffusion de documents scientifiques de niveau recherche, publiés ou non, émanant des établissements d'enseignement et de recherche français ou étrangers, des laboratoires publics ou privés.

The Meillers Autunian hydrothermal chalcedony: first evidence of a ~295 Ma auriferous epithermal sinter in the French Massif Central

E. Marcoux[a], P. Le Berre[b] and A. Cocherie[b]

[a] *ISTO Géosciences University of Orléans, BP 6759, 45067, Orléans cedex 2, France*
[b] *BRGM 3, Avenue Claude Guillemin, 45060, Orléans cedex 2, France*

Abstract

The Meillers "quartzite" deposit represents a major hydrothermal siliceous sinter, some 50 m thick and covering an area of some 30 ha within Autunian sandstone of the northern Massif Central. This siliceous sinter comprises three facies of microcrystalline quartz: (i) a dark-colored facies (black chalcedony), locally rich in pyrite, at the base, (ii) a gray-brown fairly massive facies (gray-brown chalcedony) in the middle; and (iii) a white, finely banded, facies (white chalcedony) at the top. Orientation measurements of the banding have revealed the paleo-flow channels of the silica-saturated fluids. The geochemistry of the deposits shows modest metal values, in particular for gold (average of 0.58 g/t Au, giving a gold metal content of some 20 t). The hydrothermal event is stratigraphically well correlated with the basal Autunian (around 295 Ma); an age that has been confirmed through radiochronological determination (300±21 Ma; SHRIMP on hydrothermal zircon). The lead isotopic composition is not very radiogenic ($^{206}Pb/^{204}Pb$=18.20) and is similar to that of the Late Hercynian gold lodes in the Massif Central. The mineralized sinter appears to have derived from a geyser-type hot springs. This hydrothermal activity coincides with the auriferous metallogenic peak that occurred in the Hercynides around 300 Ma. This is the first known epithermal-type surface manifestation described for the Hercynian gold event.

Author Keywords: Meillers; Massif Central; France; Sinter; Silica; Epithermal; SHRIMP; Hercynian

1. Introduction

The industrial group CERF is currently quarrying a silica deposit under the name "Meillers quartzite" destined primarily for the production of silicocalcium and ferrosilicium by Péchiney's electrometallurgical branch. The aim of the present study was to improve our knowledge of this geological feature, which

is, as far as we know, unique in the Massif Central. We therefore undertook as complete an investigation as possible (i.e., determination of extent, morphology, mineralogy, geochemistry and SHRIMP dating on zircon) so as to be able to place the silica deposit within the geological and metallogenic context of the Massif Central.

2. Geological Setting

2.1. Regional Geology

The deposit is located near the village of Meillers, in the Allier Department, 18 km west of Moulins and 6 km west of Souvigny, in the northern part of the Massif Central (Fig. 1) (deposit location: 46°30′52″N, 3°5′38″E). It forms an elongate wooded butte that stands out in the landscape and, where richest in silica, supports a stunted vegetation of heather and holly.

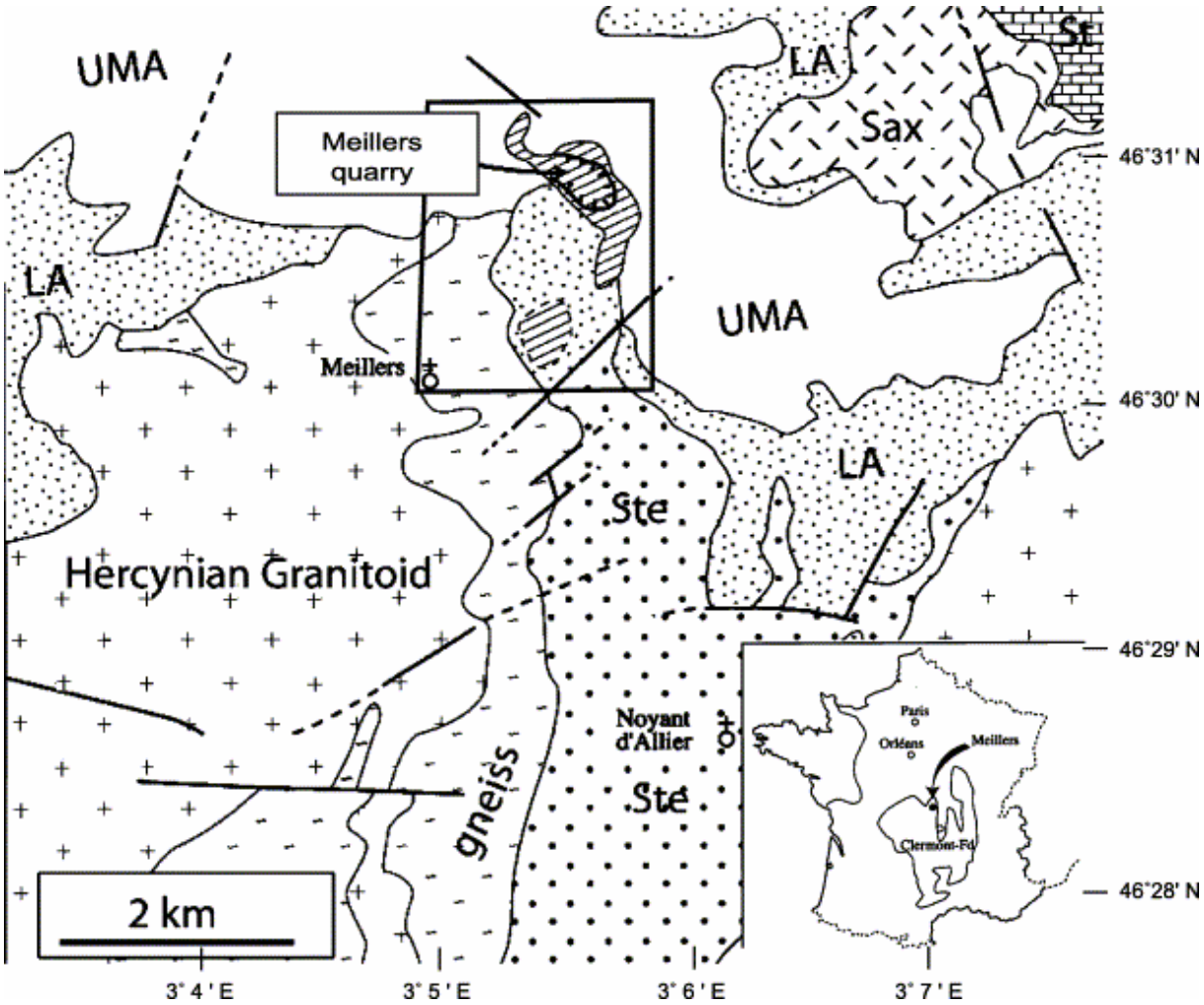


Fig. 1. Geological sketch map showing the location of the Meillers silica deposits (hatched areas). St: Stampian (35 Ma) limestones; Sax: Saxonian (260–275 Ma) sandstones; UMA: Upper-Middle Autunian ("Autunien rouge" 275–285 Ma) sandstones and shales; LA: Lower Autunian ("Autunien gris" 285–295 Ma) sandstones and shales; Ste: Stephanian pelite, arkose and conglomerate. Marked area refers to Fig. 2.

The deposit was first described by Boulanger (1844), De Launay, and later Randoin (1940) in the Explanatory notes to the 1:80,000-scale geological map. Later, Deschamps (1968) (in Debriette 1985) studied the deposit and attributed a hydrothermal origin. These early investigations, as well as all the geological work carried out on site by the quarry operator, were re-examined and synthesized by Turland (1990) for the 1:50,000-scale Bourbon-l'Archambaud geological map. Due to this hydrothermal origin, we decided to refer to the silica cap of Meillers using the modern term of "sinter" or siliceous sinter. The deposit occurs on the mylonitized western border of the Permian-Carboniferous Queune (or Noyant) Basin, in the extreme north of the Coal Belt (*Sillon Houiller*), where the underlying Paleozoic rocks have been affected by the Hercynian orogeny. The basin, itself, is bounded by basement rocks represented by the Hercynian calc-alkaline Trében granite to the east and Montmarault granite to the west.

Sedimentation began during the Middle Stephanian with conglomerates containing basement clasts, which were followed by arkose and variably carbonaceous pelite with coal beds. The sedimentation style was rhythmic, deposited in restricted sequences and is considered to have originated from the immediate basin edges with little reworking or transport. It was accompanied by intense explosive volcanic activity with the extrusion of calc-alkaline trachybasaltic lavas. The presence of rhyolitic clasts in the basal conglomerates of the Stephanian also suggests the existence of an early, pre-Stephanian, felsic volcanism.

A phase of E–W compression during the Late Stephanian (Bourbonnais orogenic phase) ended the sedimentation, folded the sediments and gave rise to a cataclasis of the basement. This period is marked by the sub-horizontal Autunian unconformity on the folded or almost vertically dipping Stephanian. The onset of an extensional regime with a conjugate system of NE–SW and NW–SE faults resulted, during both the Early Autunian (*Autunien gris*) and the Middle to Late Autunian (*Autunien rouge*), in renewed but spasmodic sedimentation with the arrival of continental sandy-pelitic sediments and bituminous shales deposited under reducing conditions in limnic basins. This sedimentation was accompanied by a discrete calc-alkaline volcanism mainly marked by layers of ash tuff.

Post-Saxonian deposits are poorly characterized. During Triassic and Jurassic, the geological history of the region was marked (a) by a marine transgression from the north and (b) by a halt in sedimentation with continental weathering of the basement until the Eocene. At the end of the Eocene, we notice the development of tropical pisolitic ferruginous soils under a dry climate and, during the Oligocene, subsidence of the Limagnes accompanied by the accumulation of continental sediments with dominant limestone.

2.2. The Meillers silica deposit

The silicification at the Meillers deposit is assigned to the Autunian (295–275 Ma) on the basis of stratigraphic and palynological evidence (Turland, 1990). Stratigraphically, this event affected beds assigned to the basal Autunian (*Autunien gris*) comprising coarse-grained sandstone with carbonaceous veins (Turland, 1990), which is consistent with an absence of the folding that is locally common in the Stephanian. In addition, the earlier authors (op. cit.) mention an interstratification of the siliceous lens within the basal Autunian sandstone and conclude a contemporaneity of the silicification with the deposition of the Lower Autunian beds; the Renière sandstone (*Autunien gris*) unconformably overlies the hydrothermal silica deposit via a 1–2-m-thick breccia with angular clasts of white, banded chalcedony. This breccia is seen in scattered blocks disseminated in the forest north and east of the quarry and near high 411 to the south (Fig. 2): it thus marks the boundaries of the silica deposit lens at the surface.

Paleontological studies revealed the presence of Late Paleozoic plant remains (*Psaronicus*, fructiform spikes), as well as silicified ostracods in the white chalcedony of the silica deposit.

The excavation of the quarry faces provided new observations that confirm the Autunian age of the hydrothermal silicification. In the first place, the northern, eastern and southern edges of the quarry (cf. sites A and B in Fig. 3) show the in situ summital breccia as a conformable m-thick layer of conglomeratic sandstone with cm-size clasts of hydrothermal silica under which we find a white, banded chalcedony. Secondly, the abandoned part of the North Quarry (cf. site C of Fig. 3) shows a conformable lenticular bed, with a maximum thickness of 1.5 m, of non-silicified detrital sandstone intercalated between a white chalcedony above and a gray-brown chalcedony below (the two main facies of the silica deposit).

This bed, visible over some 10 m, contains small pebbles (2 cm maximum) of white chalcedony, indicating contemporaneity with hydrothermal activity. Both sites are in an identical stratigraphic position and reflect the interruption of the hydrothermal deposition by the fairly abrupt onset of detrital sedimentation, probably of fluvial origin since channel structures are visible.

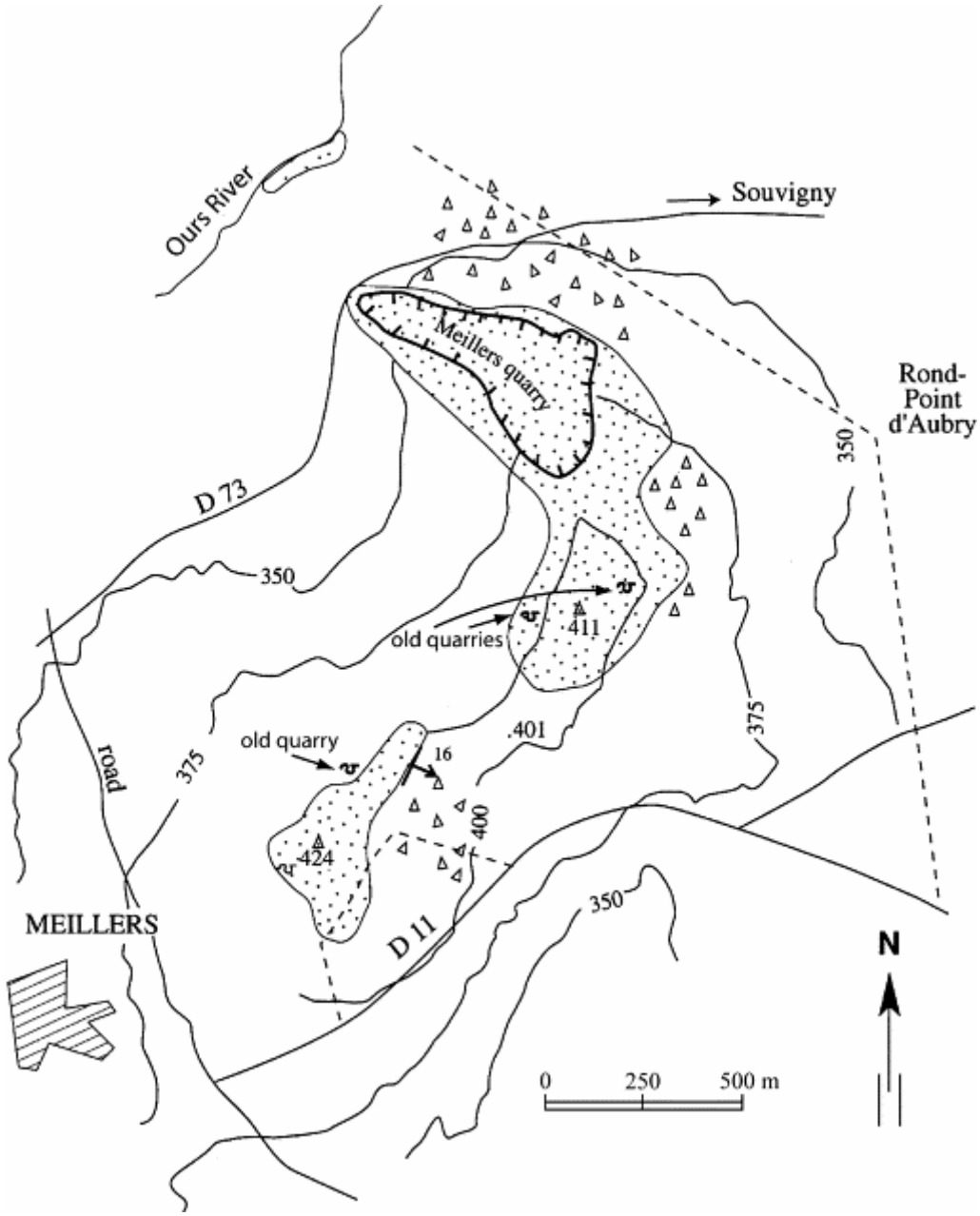


Fig. 2. The Meillers siliceous area. Stippled areas represent silica sinters extensions of the northern and southern deposit, located at topographic highs. Bold arrow indicates dip and strike of flow banding in the southern deposit. Triangles show zones with numerous conglomeratic sandstone boulders with silica fragments, surrounding silica deposits.

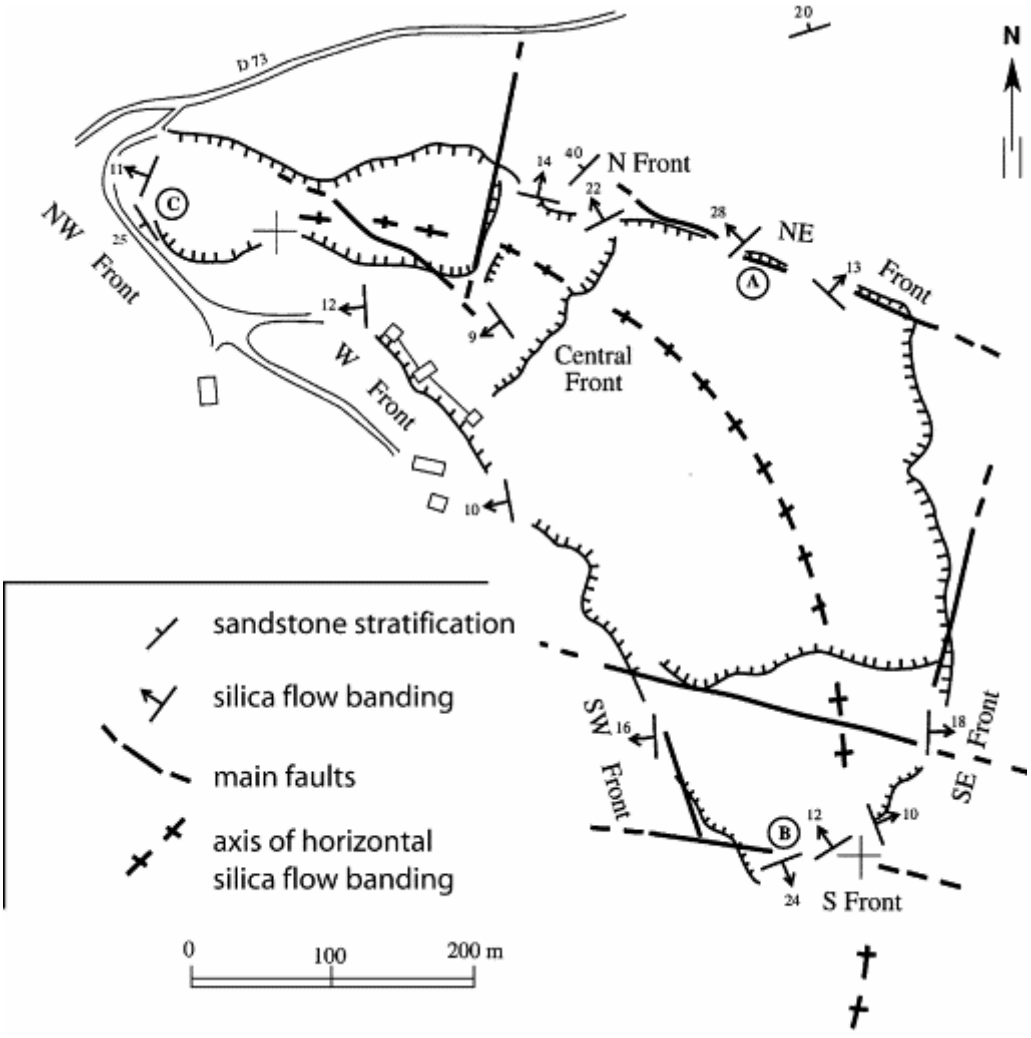


Fig. 3. Sketch map of the quarry showing the orientation of the silica flow banding in the quarry.

3. Mine geology

3.1. General features

The size of the Meillers sinter ["quartzite"] quarry is about 700 m by 250 m, i.e., an area of some 0.2 km^2 (Fig. 2). The sinter nevertheless continues southward for almost 400 m to beyond the high at 411 m, which could correspond to the main center of the hot spring deposition on activity. Northwards, however, the deposit disappears within a very short distance, even though one finds sparse zones of smaller sinters up to the Ours river, 250 m to the north.

The main siliceous sinter forms a lens with common and clear sub-horizontal laminations. Its thickness is generally estimated at 50 m because, even though the lens has been intersected by a number of 20–30-m-long drill holes, these were stopped before crossing the entire body. The best information on the thickness is provided by the working levels that extend between 362 and 402

m, i.e., over a vertical thickness of 40 m. This is a minimum thickness because the base of the lower working level always remains within the silica, but in a gray-brown chalcedony facies that is low quality from the commercial standpoint. The volume of exploitable silica in this sinter lens is around 30–36 Mt.

A second silica deposit is found some 600 m to the southwest at the 424 m high (Fig. 2). From this site, the blocks of banded hydrothermal chalcedony continue for some 400 m along a N 40 E axis, which seems to correspond to a silicified fracture zone. This secondary lens does not, however, join up with the main lens worked by the quarry. Two short drill holes recently (in 2000) investigated this secondary lens near the top of the southern butte (peak 424). Unfortunately, they were stopped after intersecting 7 m of white chalcedony, and therefore provide no accurate data concerning the thickness of this second lens.

We have no data that indicate either the existence or the emplacement of one (or more) possible eruptive craters that would have enabled the surface discharge of hydrothermal fluids.

Nowhere is the main sinter lens very fractured, and the horizontal banding shows little disturbance, which is consistent with a cessation of Hercynian deformation at this period. This regularity is a favorable factor for quarrying. Systematic measurements of the banding were made at the working faces. Although everywhere shallow (less than 30° and commonly less than 10°), the dip nevertheless allowed us to determine the flow directions of the siliceous fluids (Fig. 3 and Fig. 4). The fluids flowed first in a northerly direction from point 411, before veering to the northwest in the middle of the quarry, very likely, in a paleovalley; we are thus in a situation of inverted relief. Two fracture systems affect the sinter (Fig. 3). The main system, marked by a zone of reddening and argillization, comprises normal faults trending N 90–105° E with a sub-vertical to steep southerly dip; these are commonly filled by comb quartz, with pyrite, barite and fluorite having also been reported (Turland, 1990). The N 90–105° E strike is also that of the mineralized veins (fluorite, barite, quartz and sulphides) that cut the regional granite massifs (Montalimbert, La Croix Blanche).

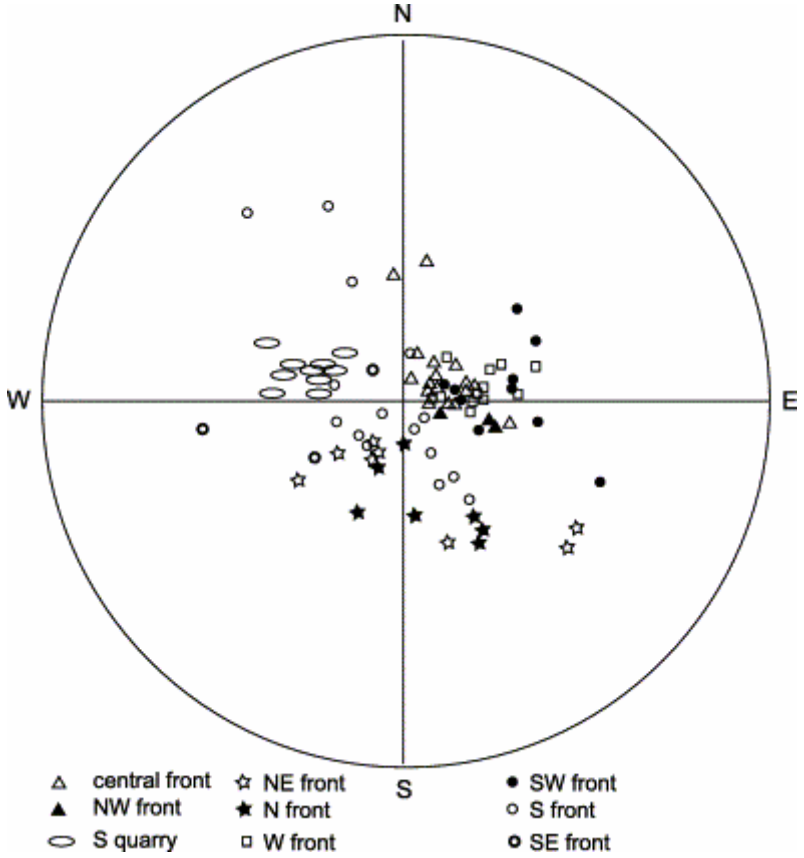


Fig. 4. Stereogram of the silica flow banding

The second fracture system varies between N 140° and 180° E, with the largest fractures trending around N 180° E with a steep easterly dip. These faults are earlier than those of the main system and are generally marked by hydraulic fracturing and a fill of white clay (regular type R3 interlayered illite/smectite with 85–87% illite). The faults are locally occupied by clastic dikes or networks of siliceous veinlets cross-cutting all the facies. They are interpreted as initially synsedimentary faults that were reactivated at several periods and that formed inflow channels for the silica. This type of fault is probably related to the conjugate NW–SE and NE–SW faults that formed during the Autunian with the emplacement of the extensional regimes, having given rise to instability on the western border of the Noyant Basin where the Meillers deposit is located. Other than the probably meteoric argillization and major silicification of the sandstone, no hydrothermal alteration has been seen in the siliceous sinter. This absence can be attributed to the hypersiliceous and non-aluminous character of the environment, consisting of dominant siliceous sandstones.

3.2. Industrial processing

The "quartzite" destined for electrometallurgical use is simply crushed, screened, washed and delivered as 40/130 mm aggregate. Two qualities are produced: a standard quality (less than 0.35% Al and 0.15% Ti) and a superior

quality (less than 0.20% Al and 0.085% Ti). Further washing is often necessary, particularly for the manufacture of superior quality silica.

Part of the production (particle size <30 mm) is marketed for the manufacture of cement and rock wool and for road surfacing. Total production is of the order of 70,000 to 80,000 t/year, of which 50,000 to 60,000 t/year for electrometallurgy (70% of the tonnage, but 90% of the value). The workable layer has been tested over a thickness varying between 7 and 30 m (thicker in the north) with a small overburden thickness of between 0 and 2 m. The reserves of workable material are estimated (1999) at 4–5 Mt of which 20% is of superior quality (i.e., 800,000 t) and 80% of standard quality.

4. Stratigraphy and petrography

Study of the quarry faces and drill hole cores has enabled us to draw up a stratigraphy for the siliceous sinter, marked by three different facies, which are from top to bottom:

Facies 1: white banded chalcedony that can often be subdivided into a 2–3-m-thick basal facies composed of massive milky beds with small vugs, overlain by a 3–10-m-thick facies with a finely laminated structure that lends its cachet to the Meillers deposit (Fig. 5A and B).
Facies 2: grey-brown chalcedony, which is 5- to 15-m thick depending on the location (Fig. 5C).
Facies 3: black chalcedony with sulphides found mainly at the base of the siliceous sinter where it is next to non-silicified sequences of sandstone. Its thickness is of the order of 10 m (Fig. 5D).

The lens is overlain by an erosive unit (1 to 2 m) of conglomerate with angular and rounded clasts mainly of white, banded chalcedony in a fine-grained silica cement containing an increasingly large amount of detrital material.

The "stratigraphic" sequence is not, however, constant and the drill holes commonly intersect intercalations of white, banded chalcedony within the gray-brown chalcedony, or sandy-conglomeratic intercalations indicating local dismantling of the siliceous sinter. This stratigraphy confirms the rhythmic pattern of the hydrothermal deposits, which could have alternated with sedimentary deposits to end with a major deposition of white, banded chalcedony forming the thickest facies. This white, banded chalcedony of the topmost facies provides the superior quality product.

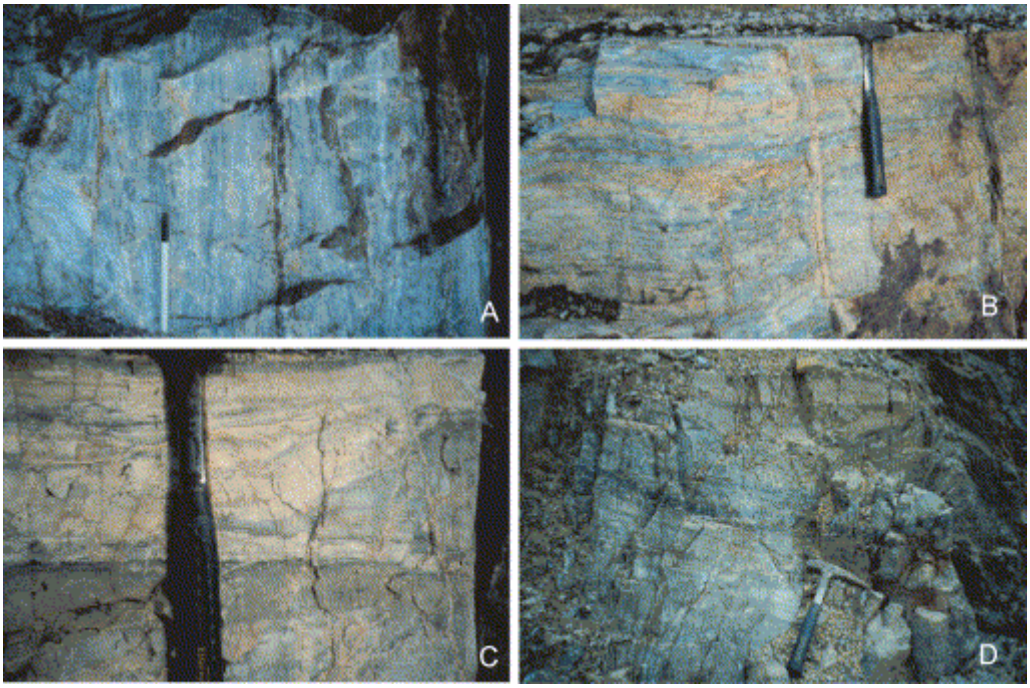


Fig. 5. Main facies of Meillers silica deposit. (A) Extracted block of white chalcedony: normal facies showing fine laminations. (B) White chalcedony in outcrop, crosscut by late quartz veinlets. (C) Block in outcrop showing a sharp contact between white chalcedony (upper part) and gray-brown chalcedony (lower part). (D) Lower part of the gray-brown chalcedony facies, still showing thin laminations of black chalcedony. Lower part of the quarry.

5. Mineralogy and geochemistry

5.1. Mineralogy

The three siliceous facies making up the deposit have distinct mineralogical features. Quartz is obviously the largely dominant mineral phase (everywhere more than 95%). As it has been shown that sinters older than 50,000 years have totally recrystallized to microcrystalline quartz (Herdianita et al., 2000), whatever the precise age of Meillers sinter, it is too old to expect the opal to have been preserved. The laminated, and probably in places in pillar and floor textures have, however, seem been locally preserved (Fig. 6).



Fig. 6. Probable preserved pillar and floor texture in white, banded chalcedony.

The white, banded chalcedony at the top has a porcelain-like aspect and a fairly constant finely laminated texture passing locally to more massive facies; opal is nowhere seen. This original lamination occurs at two scales; the one millimetric (2 to 5 laminae per cm) and the other metric with stacks of laminae cutting the sinter into poorly individualized dm-thick subhorizontal beds, in places marked separated by a thin clayey fill. Common microgeodes, with quartz crystals and a maximum length of 4 cm, lie parallel to the banding. Under the microscope, the white, banded chalcedony appears to comprise microcrystalline quartz with rare opaque minerals of the same size. The banding is due to the alternation of fine-grained (1 to 10 µm) and coarser grained (patches of 10 to 50 µm) layers, the bedding being commonly marked by concentrations of opaque minerals (Fig. 7).



Fig. 7. Banding of the white, banded chalcedony, well marked by concentration of heavy minerals (width of photo: 150 µm).

The banding commonly shows festoon or cauliflower structures suggestive of an organic deposition (Fig. 8). Moreover, sedimentation structures such as funnels and fluid escape structures Vermiculate structures with ostracods suggesting a silicified palustrine deposit have been described in this silica deposit (Turland, 1990). The silica deposit is commonly unsorted, and it is not uncommon to see coarse clasts incorporated into a finer-grained chalcedonic facies indicating successive phases of deposition and fragmentation that occurred during the depositional process. The low grain size is typical of a chemical precipitate and could be easily designated as a chert.

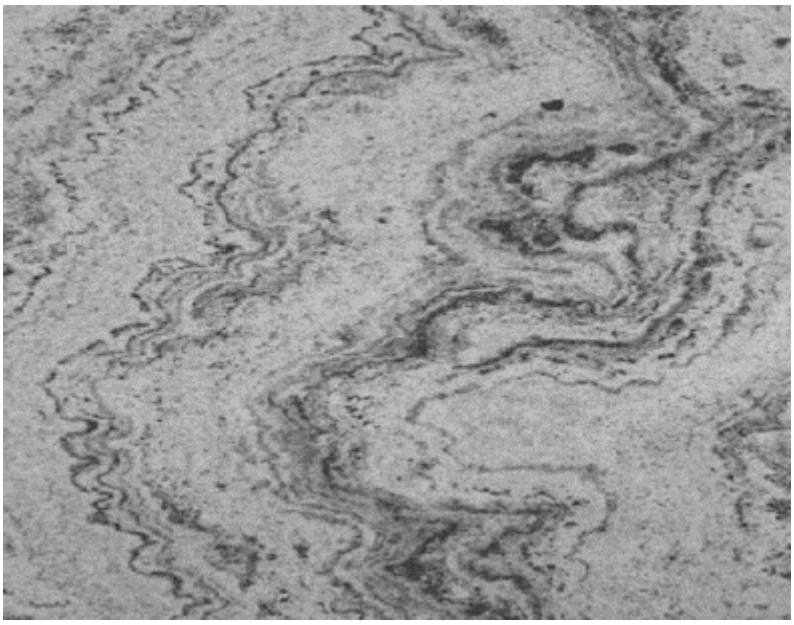


Fig. 8. Banding of white, banded chalcedony showing cauliflower structures suggestive of an organic deposition (width of photograph: 500 µm).

The "white quartzite" sometimes described in the drill-hole logs is a white to gray-white chalcedony with a grainy fracture generally containing translucid angular clasts; it is part of the white, banded chalcedonite. The gray-brown chalcedony is gray to brown (locally reddish) facies with a granose fracture and is very locally banded (lower quarry in the north) or brecciated. The facies shows cm-size vugs filled with small idiomorphic quartz crystals. The black chalcedony is not only similar to the preceding facies but also contains a large proportion of black pyrite–marcasite-rich fragments. It occurs at the base of the gray-brown chalcedony and in places directly below the white, banded chalcedony. It is essentially present in the lower quarry (north of the exploitation) where the deep parts of the silica sinter were worked. It is commonly invaded by white chalcedony (Fig. 5D).

Grey brown and black facies include a major terrigenous fraction that appears as thin layers silicified by a microcrystalline cement, or as layers preserved from silicification.

Under the microscope, the gray-brown and black facies are very similar, both being characterized by the presence of detrital fragments of 0.5 to 2.0 mm diameter, generally composed of interlocking crystals of quartz (50 to 200 µm) dispersed in a matrix of microcrystalline quartz (1 to 10 µm). This matrix contains opaque granules, in places distributed around the edges of the coarse fragments to which they impart a darker color.

Study of the quarry shows that silica deposition was interrupted by episodes of fracturing. These commonly comprise sub-vertical breccia dikes about a dm thick, with angular fragments of sandstone or gray-brown chalcedony supported by a fine-grained matrix of finely banded, white chalcedony, and in places of clay. Black chalcedony commonly occurs along synsedimentary normal faults, cross-cutting the banding of the grey-brown chalcedony. All three chalcedony facies are crosscut by a network of mm- to cm-thick veinlets of very steeply dipping quartz.

5.2. Geochemistry of the three chalcedony facies

The Meillers "quartzite" used for the manufacture of ferrosilicium must respond to the chemical constraints imposed by the clients, and in particular to the accepted levels of Fe, Al, and Ti. The average concentrations of these elements in the different facies are given in Table 1. The zones of very high purity (southern part of the quarry) everywhere correspond to the white banded chalcedony with average grades of 99.0% SiO_2, 0.21% Al_2O_3, 0.09% Fe_2O_3 and 0.036 TiO_2 (averages obtained from selected samples: they cannot be transposed to all the banded white chalcedony facies). The iron content is everywhere high in the black chalcedony, and to a lesser degree in the grey-brown chalcedony (Table 1).

	Number of analyses	SiO_2	Fe_2O_3	Al_2O_3	TiO_2
White banded chalcedony	325	98.63 ± 0.54	0.14 ± 0.20	0.29 ± 0.23	0.13 ± 0.07
Grey-brown chalcedony	277	97.17 ± 2.38	0.31 ± 0.38	1.02 ± 1.37	0.29 ± 0.13
Black chalcedony	95	95.68 ± 4.05	0.88 ± 1.25	1.42 ± 1.68	0.33 ± 0.13

Table 1. Geochemistry of the main chalcedony facies: major elements (XRF analyses, BRGM, Orléans)

Multielement analyses (Table 2) have also shown fairly systematic and not insignificant values for certain trace elements: Sr (9 to 323 ppm), Sb (10 to 260 ppm), Ba (10 to 504 ppm), Zr (<20 to 128 ppm), and more erratic values for Pb, As and Li. Moreover, all the analyzed samples contain gold values ranging from 20 to 2370 ppb, the weighted mean being 582 ppb. Accepting that this weighted mean is representative of the average grade of the sinter, the quantity of gold contained in the Meillers siliceous deposit ("quartzite") would be about 20 t. Calculations of the mean and standard deviation show that the gold grades are very uneven within the deposit and even within an individual facies (Table 2). The highest grades (>2.3 ppm) are found in the breccia dikes and also in the white, banded chalcedony (a single value of

1759 ppm), so that no facies can be considered as particularly rich in gold. There is also a fairly good Sb–Au correlation (Fig. 9).

Sample	Li (ppm)	As (ppm)	Sr (ppm)	Ag (ppm)	Au (ppb)	Sb (ppm)	Ba (ppm)	W (ppm)	Pb (ppm)	Zr (ppm)
White banded chalcedony	na	na	23	2	1759	121	22	na	22	<20
White banded chalcedony	na	na	23	1.3	153	38	77	na	12	<20
White banded chalcedony	na	na	20	0.7	103	56	20	na	15	<20
White banded chalcedony	22	<20	27	8.8	888	129	142	34	<10	102
White banded chalcedony	<10	<20	12	1.5	77	43	34	<10	<10	37
White banded chalcedony	<10	<20	13	<0.2	1282	145	31	14	<10	54
White banded chalcedony	<10	<20	10	<0.2	1490	56	22	<10	<10	<20
White banded chalcedony	22	<20	25	<0.2	219	57	56	<10	<10	<20
White banded chalcedony	13	<20	9	1.3	631	121	10	<10	<10	<20
White banded chalcedony	<10	<20	12	<0.2	1102	67	42	30	<10	25
White banded chalcedony	105	29	39	<0.2	73	41	202	<10	<10	<20
White banded chalcedony	<10	<20	10	<0.2	20	28	28	<10	<10	<20
White banded chalcedony	21	<20	19	6.1	432	106	73	15	<10	61
White banded chalcedony	57	36	48	6.6	763	129	162	19	31	56
White banded chalcedony	13	35	14	0.5	37	105	89	27	<10	61
White banded chalcedony	<10	27	15	0.2	549	142	115	21	<10	25
White banded chalcedony	<10	20	17	0.5	554	197	136	29	<10	35
White banded chalcedony	<10	<20	18	0.6	361	222	95	33	<10	28
White banded chalcedony	49	<20	30	<0.2	241	61	42	24	<10	70
White banded chalcedony	40	<20	19	<0.2	233	73	30	82	<10	23
White banded chalcedony	59	<20	32	<0.2	791	31	31	26	13	57
White banded chalcedony	27	<20	16	<0.2	87	86	23	10	<10	<20
White banded chalcedony	57	<20	18	<0.2	136	49	18	<10	<10	<20
White banded chalcedony	51	22	21	<0.2	258	45	17	<10	<10	<20
White banded chalcedony	71	40	32	<0.2	628	48	21	11	<10	<20
White banded chalcedony	47	21	17	<0.2	325	81	17	<10	<10	<20
White banded chalcedony	43	<20	12	<0.2	166	43	<10	<10	<10	<20
White banded chalcedony	67	24	18	0.3	674	52	25	94	<10	<20
White banded chalcedony	69	21	24	<0.2	336	65	51	15	16	33
White-grey chalcedony	54	27	21	<0.2	459	44	70	19	<10	56
White-grey chalcedony	60	38	22	1.7	674	73	63	<10	30	50
White-grey chalcedony	71	38	30	2.1	685	81	57	<10	39	48
White-grey chalcedony	96	<20	28	2.7	466	57	57	<10	28	36
White-grey chalcedony	46	<20	28	<0.2	568	19	85	18	15	59
White-grey chalcedony	11	<20	21	1	693	203	101	45	<10	90
White-grey chalcedony	23	<20	39	3	849	138	188	36	18	60
Average (n = 36)	47.8	29.1	21.7	2.3	521.2	84.8	64.3	30.1	21.7	50.8

	Li (ppm)	As (ppm)	Sr (ppm)	Ag (ppm)	Sb (ppm)	Ba (ppm)	W (ppm)	Pb (ppm)	Zr (ppm)	Au (ppb)
Grey-brown chalcedony	79	<20	76	0.2	21	166	60	83	128	229
Grey-brown chalcedony	37	<20	88	<0.2	10	169	21	25	85	22
Grey-brown chalcedony	21	53	27	<0.2	46	90	<10	25	58	980
Grey-brown chalcedony	21	<20	27	1	33	58	14	<10	35	66
Grey-brown chalcedony	<10	<20	12	<0.2	73	102	46	<10	105	94
Grey-brown chalcedony	27	<20	33	2.8	179	154	40	<10	55	974
Grey-brown chalcedony	16	<20	27	5.8	135	119	55	<10	123	1723
Grey-brown chalcedony	27	23	40	2.3	138	166	53	111	120	642
Grey-brown chalcedony	19	28	50	3.2	260	103	45	217	93	1415
Average (n = 9)	30.9	34.7	42.2	2.6	99.4	125.2	41.8	92.2	89.1	682.8
black chalcedony			18	2.5	67	23		16	<20	235
Black chalcedony			33	4	79	183		19	89	601

(continued on next page)

	Li (ppm)	As (ppm)	Sr (ppm)	Ag (ppm)	Sb (ppm)	Ba (ppm)	W (ppm)	Pb (ppm)	Zr (ppm)	Au (ppb)
Black chalcedony	72	65	153	9.4	121	455	42	45	108	666
Black chalcedony	25	< 20	30	8	143	191	77	17	102	226
Black chalcedony	14	< 20	19	4	72	139	102	< 10	115	75
Black chalcedony	64	147	45	3.1	116	386	< 10	27	63	269
Black chalcedony	25	24	49	2.3	63	137	< 10	80	98	777
Black chalcedony	68	44	39	1.9	68	142	< 10	27	44	356
Black chalcedony	55	24	52	2	49	259	11	21	107	415
Black chalcedony	53	63	46	3.2	56	478	< 10	23	89	604
Black chalcedony	24	47	47	2.8	167	101	47	103	123	788
Black chalcedony	31	91	53	4.3	257	154	46	63	75	874
Average (n=12)	43.1	63.1	48.7	4.0	104.8	220.7	54.2	40.1	92.1	490.5
Breccia dike	nd	nd	52	2.5	267	164	nd	54	85	2370
Breccia dike	41	< 20	49	0.5	88	201	57	44	110	439
Breccia dike	112	67	25	<0.2	40	46	< 10	172	23	62
Breccia dike	18	61	37	<0.2	208	191	40	22	127	1828
Breccia dike	51	33	153	0.6	112	434	39	73	83	471
Breccia dike	12	25	131	<0.2	188	138	34	19	80	1468
Breccia dike	32	31	31	3.5	70	158	38	< 10	98	207
Breccia dike	61	25	323	0.6	51	504	< 10	19	31	244
Average (n=8)	46.7	40.3	100.1	1.5	128.0	229.5	41.6	57.6	79.6	886.1
Global average (n=65)	44.4	36.7	41.1	2.7	100.5	127.9	38.7	41.2	69.2	582.8

Table 2. Geochemistry of the chalcedony facies: trace elements (XRF and ICP-MS analyses, BRGM, Orléans)
Note that in the text grey-white facies is included in white banded facies.

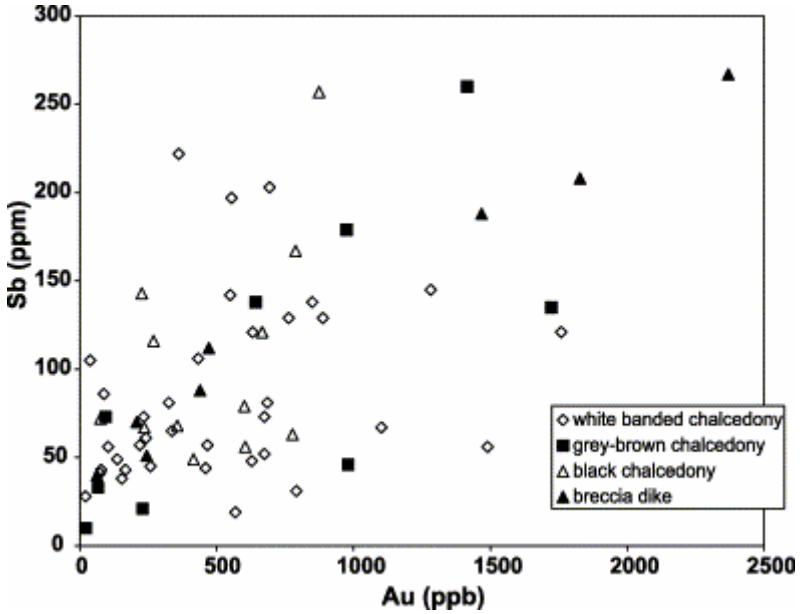


Fig. 9. Sb–Au correlation in the different siliceous facies.

The iron and titanium concentrations are due to the presence of numerous accessory minerals that are everywhere fine grained (mainly 5 to 20 µm) and highly disseminated, apart from the iron sulphides, which are relatively abundant in the lower levels of the north quarry (black chalcedony) and in the deep parts (>200 m) of the drill holes. These sulphides account for much of the high iron values encountered in the gray-brown and the black facies. They form roughly ovoid grains measuring from a fragment of 1 to 4 mm. The grains are commonly zoned and are composed of varied amounts of colloform pyrite (dominant) and squat crystals of marcasite (abundant). These two sulphides can form alternating layers in a globule or isolated

patches included in one another. The pyrite crystals commonly show well-marked cubic growth zones.

Apart from pyrite, which is very localized in the deposit, the iron concentrations are due to the presence of small crystals of hematite, and goethite, disseminated or concentrated in thin laminations that emphasize the banding. The titanium concentrations are due to the presence of small crystals (5 to 20 µm, exceptionally 100 µm) of rutile disseminated in the sinter. Ilmenite, although present, is much scarcer.

No hydrothermal aluminous mineral having been observed in the sinter, the aluminium concentrations must come mainly from local surficial argillization of the Autunian sandstones, which contain low amounts of feldspar, or from fault zones. Washing of crushed silica significantly lowers the Al content, and is sufficient for processing.

The erratic presence of sulphides (galena, sphalerite, arsenopyrite), barite, and electrum explains the metal concentrations in the siliceous sinter. These minerals are everywhere small (10 to 20 µm), apart from the sphalerite, which can attain 200 µm; one grain of gold showed a zonation with an argentiferous core. On the other hand, no antimony mineral has been seen.

The very good positive correlation between Sr and Ba shows that the Sr values are probably due to a major substitution between Sr and Ba in the barite, consistent with the existence of a complete solid solution between this mineral and celestite.

The zirconium concentrations can be explained by the presence of fairly numerous zircons ranging from 10 to 50 µm in size. Many of these minerals are euhedral with clear faces that show no erosion, attesting to their hydrothermal origin; they are mixed with more rounded zircons of probably detrital origin.

Various sinters of the Waiotapu geothermal system, New Zealand, show such a wide range of precious and base metals contents that comparisons are somewhat difficult (Hedenquist and Henley, 1985). Although the scales are not compatible, it is interesting to note that the average metal concentrations of the Meillers siliceous sinter (Pb: 41.1 ppm, Ag: 2.7 ppm) are consistent with those reported in well deposits of modern geothermal brines (Gallup, 1998). Only As (36.7 ppm), Sb (100.5 ppm) and W (38.7 ppm) appear significantly higher.

6. Geochronology and Pb isotope geochemistry

The ion microprobe technique was used to attempt to date the hydrothermal event and to distinguish it from older events recorded by detrital zircons.

6.1. Highly sensitive SHRIMP II ion microprobe determinations on zircon

Isotope measurements were performed with the SHRIMP II ion microprobe of the Australian National University at Canberra, following the analytical procedures described by Williams (1998). The analyzed spot size is 25–30 µm in diameter. Only the most homogeneous parts of the zircons, i.e., without any cracks, were investigated after detailed studies of cathodoluminescent images and reflected-light photomicrographs of sectioned zircon grains. Patches showing alteration within the zircons were not analysed, thus avoiding the less discordant zones (Krogh and Davis, 1974 and Krogh and Davis, 1975). The zircon standard AS 3 (Paces and Miller, 1993) was mounted on the same section and used for correcting the bias of the observed $^{206}Pb^{+}/^{238}U^{+}$ ratio relative to the real one. All $^{206}Pb^{*}/^{238}U$ ages were calculated to 2σ (95% confidence limit) with the Ludwig (2000) program; uncertainties are given at 1σ level (Table 3) and the error ellipse (Fig. 10) is given at same 1ó level in order to facilitate reading of the figures.

Grain. spot	U (ppm)	Th (ppm)	Th/U	Pb* (ppm)	$^{204}Pb/^{206}Pb$	f_{206} (%)	Total $^{238}U/^{206}Pb$	±	$^{207}Pb/^{206}Pb$	±	Radiogenic $^{206}Pb/^{238}U$	±	Age (Ma) $^{206}Pb/^{238}U$	±
1.1	1660	563	0.339	67	0.000328	0.59	21.273	0.141	0.0570	0.0008	0.0467	0.0003	294.4	1.9
2.1	425	569	1.340	23	–	0.06	20.266	0.174	0.0531	0.0005	0.0493	0.0004	310.3	2.6
2.2	230	254	1.105	11	0.000038	0.32	21.156	0.237	0.0548	0.0010	0.0471	0.0005	296.8	3.3
4.1	890	431	0.484	84	0.000010	0.02	9.629	0.073	0.0615	0.0003	0.1038	0.0008	636.8	4.6
5.1	387	218	0.564	36	0.000103	0.09	9.789	0.081	0.0621	0.0004	0.1021	0.0008	626.5	4.9
6.1	675	279	0.413	56	0.000012	0.06	10.668	0.082	0.0597	0.0003	0.0937	0.0007	577.2	4.3
7.1	325	225	0.694	31	0.000023	0.05	10.006	0.099	0.0606	0.0006	0.0999	0.0010	613.8	5.8
8.1	220	324	1.471	25	0.000063	0.12	10.118	0.139	0.0612	0.0006	0.0987	0.0014	606.9	8.0
9.1	*1180*	*199*	*0.168*	*83*	*0.000620*	*1.04*	*11.664*	*0.085*	*0.0665*	*0.0003*	*0.0848*	*0.0006*	*525.0*	*3.7*
10.1	*1335*	*572*	*0.428*	*42*	*0.003794*	*7.20*	*25.483*	*0.171*	*0.1083*	*0.0006*	*0.0364*	*0.0003*	*230.6*	*1.5*
11.1	*397*	*153*	*0.386*	*31*	*0.000087*	*0.40*	*11.588*	*0.093*	*0.0613*	*0.0007*	*0.0860*	*0.0007*	*531.5*	*4.1*

(1) Uncertainties given at the one σ level.
(2) f_{206} (%) denotes the percentage of ^{206}Pb that is common Pb.
(3) Correction for common Pb made using the measured $^{238}U/^{206}Pb$ and $^{207}Pb/^{206}Pb$ ratios following Tera and Wasserburg (1972) as outlined in Compston et al. (1992).

Grain. spot	U (ppm)	Th (ppm)	Th/U	Pb* (ppm)	$^{204}Pb/^{206}Pb$	f_{206} (%)	Radiogenic ratios $^{206}Pb/^{238}U$	±	$^{207}Pb/^{235}U$	±	$^{207}Pb/^{206}Pb$	±	Ages (Ma) $^{206}Pb/^{238}U$	±	$^{207}Pb/^{235}U$	±	$^{207}Pb/^{206}Pb$	±	Conc. %
3.1	646	396	0.613	97	0.000012	<0.01	0.1597	0.0012	1.582	0.015	0.0718	0.0004	955	7	963	6	998	2	96

(1) Correction for common Pb made using the measured $^{204}Pb/^{206}Pb$ ratio.
(2) For % Conc., 100% denotes a concordant analysis.

Table 3. U–Pb SHRIMP dating on zircons
Top table show results obtained on hydrothermal zircons (analyses in italic have not been considered for mean age calculations). Bottom table is for inherited zircon included in silica sinter.

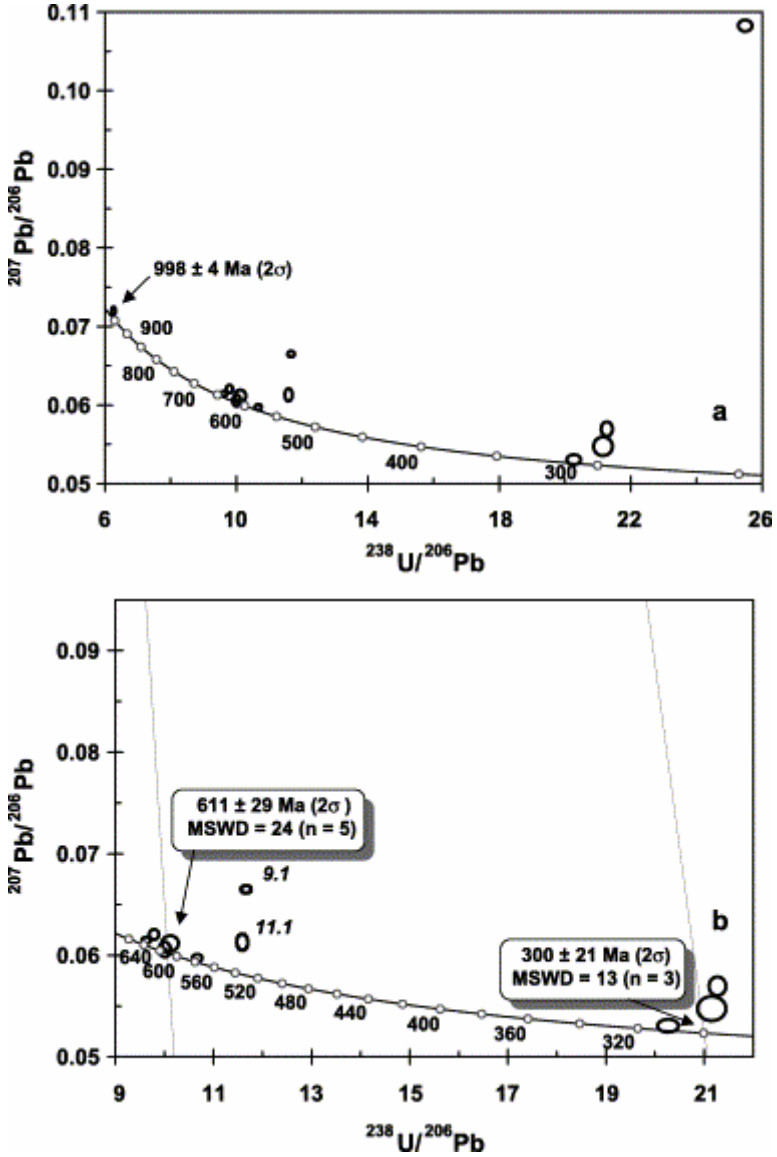


Fig. 10. (a) Tera and Wasserburg Concordia diagram for the 12 spot analyses performed on 11 zircons from the Meillers gold-bearing silica deposit—the oldest detrital zircon gives a concordant age at 998±4 Ma. (b) Age calculations for other concordant data: a group of detrital zircons around 611 Ma and a second group at 300±21 Ma are interpreted as the ages of hydrothermal events.

The $^{206}Pb/^{238}U$-calibrated data are plotted without correction for common Pb on an uncorrected version of the Concordia diagram (Tera and Wasserburg, 1972), where measured $^{207}Pb/^{206}Pb$ ratios are plotted as a function of calibrated $^{238}U/^{206}Pb$ ratios (Claoué-Long et al., 1995). Note that a Concordia diagram is much more convenient than the Wetherill (1956) diagram when plotting Phanerozoic zircons, because the $^{204}Pb/^{206}Pb$ ratio is poorly defined for such young material and a common Pb correction is critical for a $^{207}Pb/^{206}Pb$ age determination. In addition, by using well-calibrated $^{206}Pb/^{238}U$ data, the uncertainties for Phanerozoic zircons on $^{206}Pb/^{238}U$ ages are much smaller than on $^{207}Pb/^{206}Pb$ ages. The measured composition of zircons having undergone neither Pb loss, nor contamination by older inheritance, must plot on a mixing line between the $^{207}Pb/^{206}Pb$ composition of crustal Pb derived

from the two-stage Stacey and Kramers (1975) model and the totally radiogenic Pb on the Concordia curve. The closeness of the analyzed points to the Concordia is a much more precise indication of the common Pb contribution than the $^{204}Pb/^{206}Pb$ measurement, and the common Pb-corrected $^{206}Pb/^{238}U$ age is directly determined by the intercept of the mixing line with the Concordia curve. Thus, three possible trends are possible for discordant analyses: (i) the common-Pb trend, (ii) the inheritance trend, and (iii) the recent-Pb-loss trend (see Williams, 1998, after Claoué-Long et al., 1995). The recent-Pb-loss trend (along a vector parallel to the $^{238}U/^{206}Pb$ axis) and the inheritance trend are easily distinguishable from a common-Pb trend, which follows a vector almost parallel $^{207}Pb/^{206}Pb$ axis.

Only a single spot analysis was corrected for common Pb with a conventional ^{204}Pb correction (spot 3.1, Table 1) because it is significantly older than other spot analyses and it contains a high amount of U and a subsequently high level of Pb*.

The zircons were separated using the standard procedure of grinding, sieving, magnetic and density separation, and hand picking, taking care to prevent any sort of contamination during the sample preparation. The extracted grains are heterogeneous and rather small (<150 μm); they are mainly colorless and limpid, sometimes rounded. About 40 grains were selected for mounting on a polished section, and 12 spot analyses were done on 11 grains.

6.2. Results

The analyses are listed in Table 3 and the data are plotted on an uncorrected Tera and Wasserburg diagram (Fig. 10). Within the analytical uncertainty at 2σ, three analyses are clearly discordant: i.e., spot analyses 9.1, 11.1, and in particular 10.1 which shows a large common Pb contribution as indicated by the high $^{204}Pb/^{206}Pb$ ratio (0.0038). All the other analyses are concordant or subconcordant, but widely spread in age from 1000 to 300 Ma. The older age is given by the subconcordant spot (96% concordancy) at 998±4 Ma. Among the eight remaining data, two groups of points can be identified around 600 and 300 Ma (Fig. 10b). As explained in the analytical section, two types of discordant data exist: the one follows the common-Pb trend and the second indicates radiogenic-Pb loss parallel to the $^{238}U/^{206}Pb$ axis. We thus defined two common-Pb trends at 600 and 300 Ma using the values of the $^{207}Pb/^{206}Pb$ ratio, according to the Stacey and Kramers (1975) model, and the concordant or subconcordant data. The intercepts enabled us to calculate two ages, 611±29 Ma (2σ) and 300±21 Ma (2σ), which are not well constrained due to the limited number of data and their rather large range of variation—the poor quality of the statistics is shown by the high MSWD values of 24 and 13, respectively. This in situ geochronological study indicates that most of the zircon grains are of detrital origin (≈1000 and ≈600 Ma) without any relationship to the hydrothermal stage we are looking for. Only two grains

and three analytical spots yielded a Hercynian age at 300±21 Ma. Despite a high MSWD (13), this age is in complete agreement with the stratigraphic constraints and could, therefore, date the hydrothermal event.

The isotopic composition of the lead was measured on a concentrate of pyrite, which is a common mineral at the base of the sinter. The lead, uranium and thorium concentrations determined by ICP/MS are 66.3, 0.35 and 0.28 ppm, respectively. These values allow us to calculate the values of μ (0.34) and W (0.28), and to apply minimal corrections for in situ disintegration. The isotopic ratios are 18.204 ($^{206}Pb/^{204}Pb$), 15.648 ($^{207}Pb/^{204}Pb$) and 38.364 ($^{208}Pb/^{204}Pb$) (ratios corrected at 300 Ma). These not very radiogenic ratios are similar to those measured in the Late Hercynian gold deposits of the Massif Central (Touray et al., 1989).

7. Discussion

The Meillers siliceous sinter, wrongly named "quartzite", which is finely banded, especially in the upper part, with clear cherty facies, has long been recognized as being of hydrothermal origin. It corresponds to a hot-spring surface deposit similar to the siliceous sinters of present-day hydrothermal sites such as Yellowstone (Wyoming, USA) and Taupo (New Zealand). Some samples have preserved the typical pillar and floor structure, but quartz crystallization has obliterated most of it. Measurements of the banding have revealed the flow directions of the siliceous fluids. The main zone of discharge was probably located at or near peak 411, to the south of the quarry, from whence the fluids flowed northward along a paleovalley. A secondary discharge site was probably located at peak 424, farther to the south. The flow in a paleovalley would explain the thickness variations noted in the drill holes. The siliceous crust was been fragmented on several occasions under the effect of brecciation, possibly associated with hydrothermal eruptions.

The presence of a major siliceous sinter and its geochemistry (Au–Sb without As; Hg not determined) shows that, as in the Taupo Volcanic Zone and most of Yellowstone, we are dealing with the sinter of a neutral epithermal system that involved hot, neutral to slightly alkaline, solutions. The silica concentration of such fluids measured in the present-day systems (Hedenquist and Henley, 1985; Fournier, 1985 and Fournier, 1989) varies from 170 to 710 mg/kg, with an average around 400 mg/kg. Considering a silica precipitation efficiency of about 1% (Simmons, personal communication), an extended lifetime may be expected for formation of the 13×10^6 m^3 Meillers silica deposit.

Gold in these systems is deposited in the surficial parts (e.g., at Taupo, New Zealand; Hedenquist and Henley, 1985), whereas base metals precipitate at depth, early in the deposition. The deep zones at Meillers start with the probably early appearance of pyrite–marcasite about 30 m below the present-day surface, suggesting reducing conditions. It is not, however, possible to say whether these zones correspond to the system's feeder

channels since drilling only intersected the upper part of the sinter. The abundance of marcasite suggests acid conditions, and the globular texture indicates an active dynamism during deposition. The pyrite–marcasite zones could thus correspond to the paleo-mud volcanoes (areas of hot-liquid and sulphide-particle emulsion) of the current epithermal fields.

The Autunian age proposed for the silicification on the basis of stratigraphic criteria, has been confirmed by radiochronology (300±21 Ma). The Meillers hydrothermal event thus belongs to the "300 Ma" metalliferous peak that gave rise to a host of mineral deposits in the Massif Central, and in particular to Au–W–Sb deposits (Bouchot et al., 1997 and Bouchot et al., 2000) such as the Lauriéras-Le Bourneix-Cheni gold lode in the Limousin (Fig. 11). This synchronism could explain the relatively high As, Sb and W concentrations in the sinter.

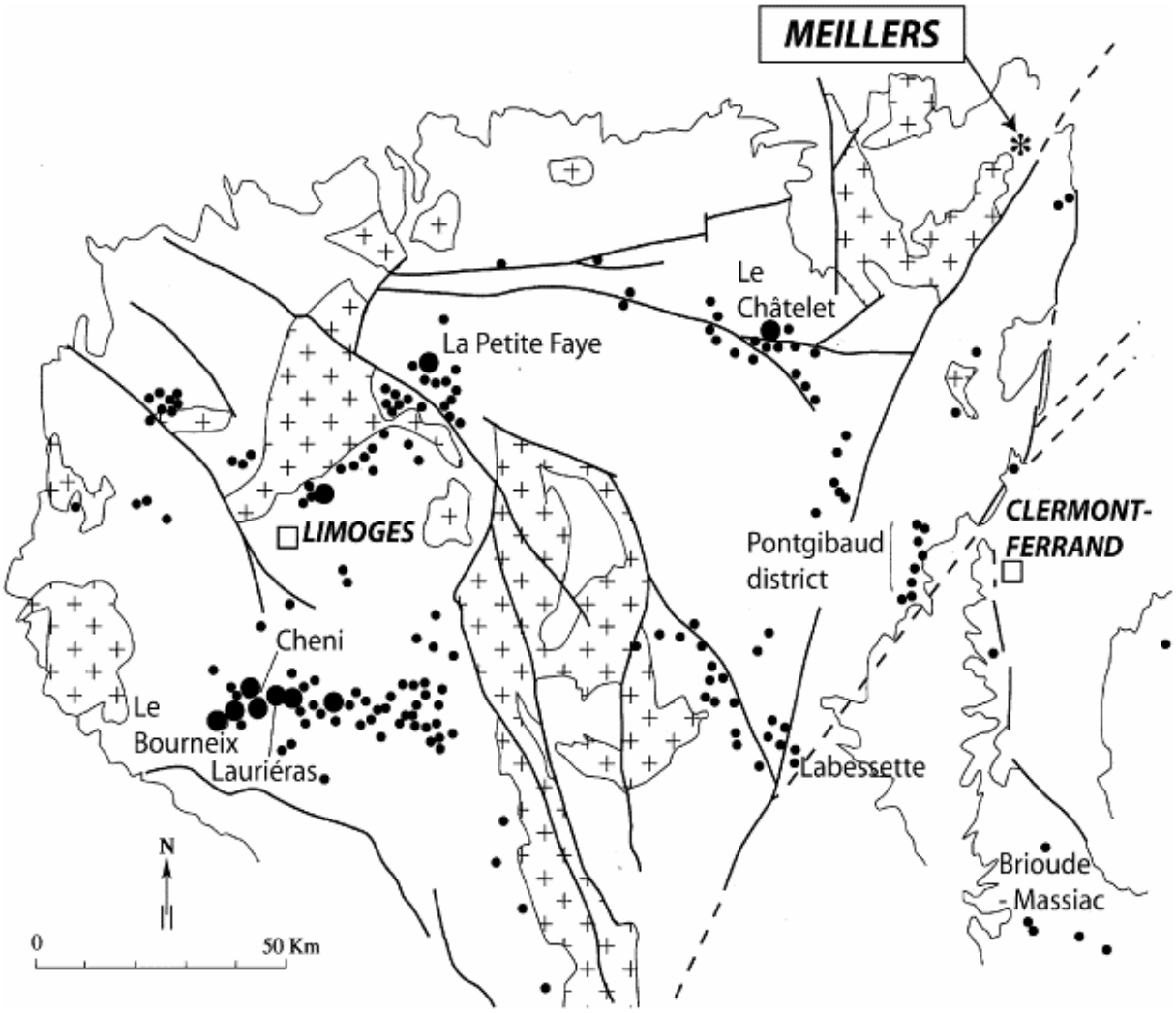


Fig. 11. Map of ~300 Ma gold deposits in the northern part of French Massif Central. Crossed areas represent Hercynian granitoïds. "Limousin" refers to the western part of the map, including Laurieras deposit and Limoges Town. Small dots refer to gold occurrences and small ore deposits (less than 10 t of gold), large dots to gold ore deposits having produced more than 10 t of gold.

Available geochronological data suggest that this metalliferous peak was relatively short lived: 5 Ma, between 310 and 305 Ma, marking a short period of transition between two phases of late orogenic extension (Bouchot et al., 2000). Despite the imprecision of the radiochronological dating, the presence of the Meillers silicification in rocks of Early Autunian age qualifies the narrowness of this peak. It is plausible that the peak, although harboring the major gold mineralization, died off gradually with a tail to 295 Ma that includes the Labessette auriferous polymetallic mineralization, the Peyrouses Sn–Au veins and other gold-bearing veinlets at Pontgibaud (Bril et al., 1991), Meillers, and possibly others (Fig. 11). This hypothesis may explain the problem of the commonly auriferous stibnite veins of the Brioude–Massiac district, the 250±10 Ma age of which (Bril et al., 1991) is under debate.

At the regional scale, the volcanic events likely to have been associated with the Meillers silicification are discrete but fairly common; ash tuffs layers in the basal Autunian (Paquette, 1980), rhyolitic crystal-and-lapilli tuff in the north and close to the Meillers "quartzite" (in Turland, 1990). Moreover, hydrothermal activity at Meillers was concurrent with the deposition of relatively coarse-grained fluvial sediments, a common surface feature of epithermal environments (for example in Oregon; Zimmerman and Larson, 1994 and Rytuba and Van Der Meulen, 1991). This once again reflects the important influence of the major Late Hercynian faults in the location of major upflow channels of gold-hydrothermal systems.

The Meillers auriferous silica deposit thus appears to be a preserved sinter of the topmost part of this generation of gold lodes that show epithermal affinities at the surface, like most "orogenic gold deposits" (Groves et al., 2000). This preservation implies very little erosion in this part of the Massif Central, unlike in the Limousin or the Cévennes. The resistance of the siliceous sinter to erosion explains the inversion of the relief and the formation of the butte in which the quarry was opened.

Acknowledgements

The Meillers deposit was studied within the framework of an RPI (Industrial Partnership Research) project between the CERF and BRGM. Major geological and industrial results are reported in Barthélémy et al. (2000). We thank Sir Patrick Skipwith Bt. for his translation of this paper. We are also indebted to C.M. Fanning of the Australian National University (Canberra, Australia) for his help in performing SHRIMP analyses, and to Stuart Simmons and James Saunders whose remarks greatly improved the manuscript.

References

Barthélémy, F., Le Berre, P., Marcoux, E., Pasquet J.-F., Récoché, G., 2000. Gîtologie et valorisation du gisement de silice de Meillers (Allier). Unpublished report BRGM/RO-50146-FR 88 pp.

Bouchot, V., Milési, J.P., Lescuyer, J.L. and Ledru, P., 1997. Les minéralisations aurifères de la France dans leur cadre géologique autour de 300 Ma. *Chronique de la Recherche Minière* **528**, pp. 13–62.

Bouchot, V., Milési, J.P. and Ledru, P., 2000. Crustal-scale hydrothermal palaeofield and related Variscan Au, Sb, W orogenic deposits at 310–305 Ma (French Massif Central, Variscan belt). *SGA News* 10, pp. 1–12 (December) .

Boulanger, C., 1844. Statistique géologique et minéralurgique du département de l'Allier. In: Moulins, Editor, , 1844. *Imprimerie Desrosiers*.

Bril, H., Bonhomme, M.G., Marcoux, E. and Baubron, J.-C., 1991. Ages K/Ar des minéralisations de Brioude-Massiac (W–Au–As–Sb; Pb–Zn), Pontgibaud (Pb–Ag; Sn) et Labessette (As–Pb–Sb–Au): place de ces districts dans l'évolution géotectonique du Massif Central Français. *Mineralium Deposita* **26**, pp. 189–198.

Claoué-Long, J.C., Compston, W., Roberts, J. and Fanning, C.M., 1995. Two Carboniferous ages: a comparison of SHRIMP zircon dating with conventional zircon ages and $^{40}Ar/^{39}Ar$ analysis. In: *Geochronology Time Scales and Global Stratigraphic CorrelationSEPM Special Publication* **vol. 54**, pp. 1–21.

Compston, W., Williams, I.S., Kirschvink, J.L., Zhang, Z. and Ma, G., 1992. Zircon U–Pb ages for Early Cambrian time scale. *Journal of the Geological Society (London)* **149**, pp. 171–184.

Debriette, J., 1985. Etude géologique du bassin permo-carbonifère de la Queune (Allier). In: *Mémoire*, DER Univ., Dijon 265 pp. .

Deschamps, J., 1968. Les formations autuno-stéphaniennes et permo-triasiques du Nord-Est du Massif central. *Revue Scientifique du Bourbonnais*, pp. 67–117.

Fournier, R.O., 1985. The behavior of silica in hydrothermal solutions. *Reviews in Economic Geology* **2**, pp. 45–62.

Fournier, R.O., 1989. Geochemistry and dynamics of the Yellowstone National Park hydrothermal system. *Annual Review of Earth and Planetary Sciences* **17**, pp. 13–53.

Gallup, D.L., 1998. Geochemistry of geothermal fluids and well scales, and potential for mineral recovery. *Ore Geology Reviews* **12**, pp. 225–236.

Groves, D.I., Goldfarb, R.J., Knox-Robinson, C.M., Ojala, J., Gardoll, S., Yun, G.Y. and Holyland, P., 2000. Late-kinematic timing of orogenic gold deposits and significance for computer-based exploration techniques with emphasis on the Yilgarn block, Western Australia. *Ore Geology Reviews* **17**, pp. 1–38.

Hedenquist, J.W. and Henley, R.W., 1985. Hydrothermal eruptions in the Waiotapu geothermal system, New Zealand: their origin, associated breccias, and relation to precious metal mineralization. *Economic Geology* **80**, pp. 1640–1668.

Herdianita, N.R., Browne, P.R.L., Rodgers, K.A. and Campbell, K.A., 2000. Mineralogical and textural changes accompanying ageing of silica sinter. *Mineralium Deposita* **35**, pp. 48–62.

Krogh, T.E. and Davis, G.L., 1974. Alteration in zircons with discordant U–Pb ages. *Carnegie Institution of Washington Year Book* **73**, pp. 560–567.

Krogh, T.E. and Davis, G.L., 1975. Alteration in zircons and differential dissolution of altered and metamict zircon. *Carnegie Institution of Washington Year Book* **74**, pp. 619–623.

Ludwig, K.R., 2000. Users manual for ISOPLOT/EX, version 2. A geochronological toolkit for Microsoft Excel. In: *Berkeley Geochronology Center Special Publication* **vol. 1a** 43 pp. .

Paces, J.B. and Miller, J.D., 1993. Precise U–Pb ages of Duluth Complex and related mafic intrusions, Northern Minnesota: geochronological insight to physical, petrogenic, and tectonomagmatic processes associated with the 1.1 Ga midcontinent rift system. *Journal of Geophysical Research* **98**, pp. 13997–14013.

Paquette, Y., 1980. Le bassin autunien de l'Aumance (Allier). Sédimentologie, charbons, cinérites ; tectonique syn-diagénétique. Thesis, University of Dijon, 277 pp.

Randoin, J., 1940. Carte géologique au 1/80 000ème de Moulins. Editions Ministère de l'Industrie, Service de la Carte Géologique de la France.

Rytuba, J.J. and Van der Meulen, D.B., 1991. Hot-spring precious-metal systems in the Lake Owyhee volcanic field, Oregon-Idaho. In: Raines, G.L., Lisle, R.E., Schafer, R.W. and Wilkinson, W.H., Editors, 1991. *Geology and Ore Deposits of the Great Basin, Symposium Proceedings* **vol. 2**, Geological Society of Nevada, Reno, pp. 1085–1096.

Stacey, J.S. and Kramers, J.D., 1975. Approximation of terrestrial lead isotope evolution by a two-stage model. *Earth and Planetary Science Letters* **26**, pp. 207–221.

Tera, F. and Wasserburg, G.J., 1972. U–Th–Pb systematics in three Apollo 14 basalts and the problem of initial Pb in lunar rocks. *Earth and Planetary Science Letters* **14**, pp. 281–304.

Touray, J-C., Marcoux, E., Hubert, P. and Proust, D., 1989. Hydrothermal process and ore-forming fluids in the Le Bourneix gold deposits, Central France. *Economic Geology* **84**, pp. 1328–1339.

Turland, M., 1990. Carte géologique au 1/50.000è de Bourbon-l'Archambaud. Editions BRGM.

Wetherill, G.W., 1956. Discordant uranium–lead ages 1. *Transactions-American Geophysical Union* **37**, pp. 320–326.

Williams, I.S., 1998. U–Th–Pb geochronology by ion microprobe. *Reviews in Economic Geology* **7**, pp. 1–35.

Zimmerman, B.S. and Larson, P.B., 1994. Epithermal gold mineralization in a fossil hot-spring system—Red Butte, Oregon. *Economic Geology* **89**, pp. 1983–2002.